



Multi-scale modeling of aerosol transport in a mouth-to-truncated bronchial tree system

Han Xiao^a, Yang Liu^a, Bingbing Sun^b, Yiyang Guo^b, Moran Wang^{a,*}

^a Department of Engineering Mechanics, Tsinghua University, Beijing, 100084, China

^b School of Chemical Engineering, Dalian University of Technology, Dalian, 116024, China

ARTICLE INFO

Keywords:

Multi-scale modeling
Aerosol transport
Respiratory tract
Network method

ABSTRACT

Computational fluid particle dynamics (CFPD) is widely employed to predict aerosol transport in a truncated bronchial tree model on account of its capacity to reveal details of flow field and particle movement. However, setting a physiologically consistent boundary condition in the CFPD for the idealized or image-based truncated bronchial tree model is still a challenge. This paper proposes a multi-scale modeling method, which contains an Extend-Bronchial tree-Network (EBN) boundary condition for a mouth-to-truncated bronchi system. The comparison between EBN boundary condition and a commonly used uniform pressure (UP) boundary condition is conducted. Subsequently, EBN method is used to study the nano-micron (100 nm–10 μm) particles transport in the mouth-to-truncated bronchi model at different inhalation volume rates (15, 60, 90 L/min). Results show that EBN method is more physiologically rational and two methods differ in flow distribution in lobes, vortex structure, and particle transport. The maximum difference in flow rate distribution in lobes between two methods is about 20 %, while the maximum relative disparity of particle penetration fraction from lobes and deposition fraction in the TLB is about 93 % and 30 %, respectively. Meanwhile, this paper reveals the variation of deposition fraction and penetration fraction with the changes in particle diameter and inhalation volume. Deposition efficiency, deposition hotspots and deposition mechanism are also analyzed with inlet Stokes number (Stk) and Reynolds number (Re). This research establishes a foundation for the simulation of aerosol transport in a whole respiratory tract and provides references for inhalation drug delivery and air pollutant management.

1. Introduction

Lung is the only internal organ within the human body that is exposed to the external environment continually [1]. Individual inhales substantial amount of air every day, that is potentially laden with pollutants such as vehicle emissions, occupational matter, as well as microbial contaminants [2–4]. As pollution intensified, respiratory diseases have been on the rise both in absolute numbers of affected individuals and in the proportion of overall disease [5]. Additionally, inhalation therapy stands as the optimal choice for treating respiratory diseases due to its ability to target the affected area swiftly and minimize systemic adverse effects [6]. Meanwhile, inhalation therapy utilizes the alveolar region for direct drug absorption into the bloodstream, bypassing first-pass metabolism in the liver. It is noninvasive and can be employed for systematic therapies [7,8].

The prediction of aerosol deposition in the respiratory tract has therefore become a significant focus on inhaled drug delivery and air

pollution prevention. The prediction methods include semi-empirical models, experimental approaches and computational fluid-particle dynamics (CFPD) simulation models [9]. Semi-empirical models, such as the ICRP model [10] and the dosimetry model, ExDoM [11], are only suitable for predicting regional deposition while their accuracy in predicting subject-specific may be limited. Experimental methods are constrained by high costs and ethical considerations. Compared to experimental and semi-empirical models, CFPD can reveal more details of the airflow field within the respiratory tract and provides more accurate site-specific predictions for particle movement with appropriate boundary conditions.

As computational power increases, the utilization of CFPD in studying aerosol transport within the respiratory tract is becoming increasingly popular. However the computational cost is still unbearable for the simulation of a whole respiratory tract since the characteristic size varies greatly from the upper respiratory tract to the bronchial tree, as well as thousands of bronchioles in the bronchial tree [12]. Therefore,

* Corresponding author.

E-mail address: mrwang@tsinghua.edu.cn (M. Wang).

<https://doi.org/10.1016/j.combiomed.2024.109292>

Received 8 May 2024; Received in revised form 8 September 2024; Accepted 15 October 2024

Available online 18 October 2024

0010-4825/© 2024 Elsevier Ltd. All rights reserved, including those for text and data mining, AI training, and similar technologies.

a common practice is to truncate the respiratory tract and simulate on the truncated model. Truncated bronchial tree models are common, not only due to the expensive computational cost of CFPD in thousands of bronchial trees but also as the resolution of CT (computed tomography) and MRI (magnetic resonance imaging) limits the establishment of high-generation bronchioles [13]. However, the truncated bronchial tree model has greater difficulty in proposing appropriate boundary conditions compared to other truncated models, as a result of multiple outlets. Two sets of common boundary conditions are utilized in previous studies. One of them involves uniform pressure at the inlet and a weighted flow rate at the truncated bronchial tree [14–17]. This type of boundary condition is usually employed in image-based models since the flow distribution is deduced from images and it varies among individuals [14,15]. The other simplified boundary condition contains uniform pressure (UP) at the truncated branch and flow rate is employed at the inlet [18–22]. This boundary condition is straightforward to implement, applicable to the idealized models, and has extensive application. Nevertheless, the assumption of uniform pressure at the low-generation bronchioles deviates from reality [23]. In recent years, several multiscale modeling methods for airflow simulation have been proposed, integrating computational fluid dynamics (CFD) for the large-sized region in the respiratory tract with a 1D impedance network model for bronchial tree [17,24,25]. These multiscale methods for airflow can be categorized into two types: image-based method and coupling algorithm-based method. In the image-based method, the inlet and outlet boundary conditions of the overall respiratory model, as well as the flow rates at various truncation points, are known. Consequently, there is no need for data transfer between different scales. In this type of coupling methods, imaging techniques are the most accurate way to determine the flow rate at truncated bronchi [17,24]. In contrast, in the coupling algorithm-based method, the pressure and flow rate at the truncated bronchi are unknown. Therefore, relying on the principle of continuity of pressure and flow at the truncation, a coupled algorithm is necessary to ensure data transfer between different scales. In the current coupling algorithm-based multiscale method, the different scales are fully coupled using a staggered coupling approach, which can sometimes be inflexible [25]. Moreover, research combining the multi-scale method with particle transport simulation is still underdevelopment and the difference between multiscale simulations and UP methods in the results of particle transport remains unclear.

The pore network model is a widely-used method for simulating transport process through porous media due to its high computational efficiency [26]. The transport process is modeled on a representative network with idealized elements. The network modeling method is applicable not only to tube networks with circular cross-sections but also to networks where the local cross-sections vary significantly, such as in diseased airways. This paper proposes a multi-scale method, termed as Extended-Bronchial tree-Network (EBN), for modeling particle transport in a mouth-to-truncated bronchial tree system. The proposed method combines network model and CFPD. In this approach, the network model is employed to predict airflow within the bronchial tree and to establish the pressure-flow rate correlation at the truncated bronchi, providing boundary conditions for CFPD in a mouth-to-truncated bronchi model. The multi-scale coupling approach in this study is more flexible than the previous coupling algorithm-based method, as the 3D and 1D simulations are conducted on separate platforms and a correlation-based approach is employed to effectively reduce the complexity of coupling algorithm. Meanwhile, it is also applicable to idealized respiratory tract models. Furthermore, this study employs EBN method to study aerosol transport in a mouth-to-lobar bronchi model. The differences between the results of EBN boundary condition and UP boundary condition are clarified. Moreover, the effects of particle diameters and inhalation volumes on particle transport within the truncated respiratory tract, as well as the deposition hotspots and deposition mechanism are revealed. This work provides a reference for the optimization of drug delivery, targeted therapy, the prevention and control

of pollutants. It also lays a foundation for the simulation of aerosol transport in a whole respiratory tract.

2. Method

2.1. Method overview

A lung changes its volume to alter the pressure difference between the alveoli and the surroundings, enabling inhalation and exhalation. In this method, uniform pressure at the terminal bronchioles (alveolar pressure) is assumed to be uniform and the aerosol is inhaled at the volume flow rate of Q_{in} . The diagram of the EBN method is illustrated in Fig. 1(a).

In Fig. 1(b), The EBN method can be generally divided into two parts. The first part is the simulation of aerosol transport from the mouth to the truncated bronchial tree. The emphasis of this article lies in this part. Meanwhile, the second part is gas dispersion from the truncated bronchi (bronchioles) to the terminal bronchioles. In the first part, the network modeling of the bronchial tree offers the relationship between the pressure (P_{EBN}), the flow rate (Q_{EBN}), and the time at the entrance of the truncated bronchi (bronchioles), which is deduced by simulating the pressure at the truncated bronchial tree under multiple flow rates. In Fig. 1(b), 'k' denotes the number of time steps, while 'R' and 'T' represent the flow resistance and inductance, respectively. Details are in section 2.3. To satisfy the continuity of pressure and flow rate at the truncation bronchi (bronchioles), the flow rate Q_o and pressure P_o in CFPD should be equated to Q_{EBN} and P_{EBN} in the network simulation, respectively. Therefore, the relationship between P_{EBN} and Q_{EBN} will serve as the outlet boundary condition for the CFPD of aerosol transport from the mouth to the truncated branch. Details are in the subsequent section 2.4. This process will give insight into airflow fields and particle deposition from the mouth to the truncated bronchial tree model when the human body inhales aerosols at a specified inhalation flow rate Q_{in} . In the second part, when breathing at the flow rate of Q_{in} from mouth, the flow rate at the truncated bronchi (bronchioles) will serve as the boundary condition for the network model. Combining the airflow in the mouth-to-truncated bronchial tree model with the results of network modeling in the truncated bronchial tree-to-terminal bronchioles, airflow inside the nearly whole respiratory tract model will be revealed.

2.2. Multi-scale respiratory tract model establishment

In the EBN method, the respiratory tract model can be either image-based or idealized. In this study, the mouth-to-lobar bronchi model is extracted from CT images with extended outlets, as shown in Fig. 2(b). The oral to upper half of the trachea model is from an adult male while the other part is from the database of an open-source simulation package CHASTE (Cardiac, Heart, and Soft Tissue Environment) [27]. The validation of this respiratory tract model is demonstrated in Section 2.5. The truncated respiratory tract model contains oral, pharynx, larynx and trachea to lobar bronchi (TLB) segments. Meanwhile, the oral, pharynx and larynx compose the upper respiratory tract. The epiglottis is located near the junction of the pharynx and larynx, while the glottis is in the middle of the larynx, which are identified in Fig. 2(b). The direction of the mouth opening determines the anterior side of the model and the opposite side is termed as posterior side. Meanwhile, the right side and left side of the model are generally distinguished by the right lobe and left lobe, separately.

Lobar bronchi are connected to the bronchial tree of corresponding lobes which are generated using a volume-filling airway generation algorithm [28]. The bronchial tree spans over 20 generations in Horsfield order and ends at terminal bronchioles. The airways are assumed to be rigid, circular, and straight and have smooth wall. The diameter varies with the Horsfield order of the airway [29,30]. This process is achieved in CHASTE. The generated bronchial tree divided by the right upper lobe (RUL), right middle lobe and right lower lobe (RML-RLL), left upper lobe

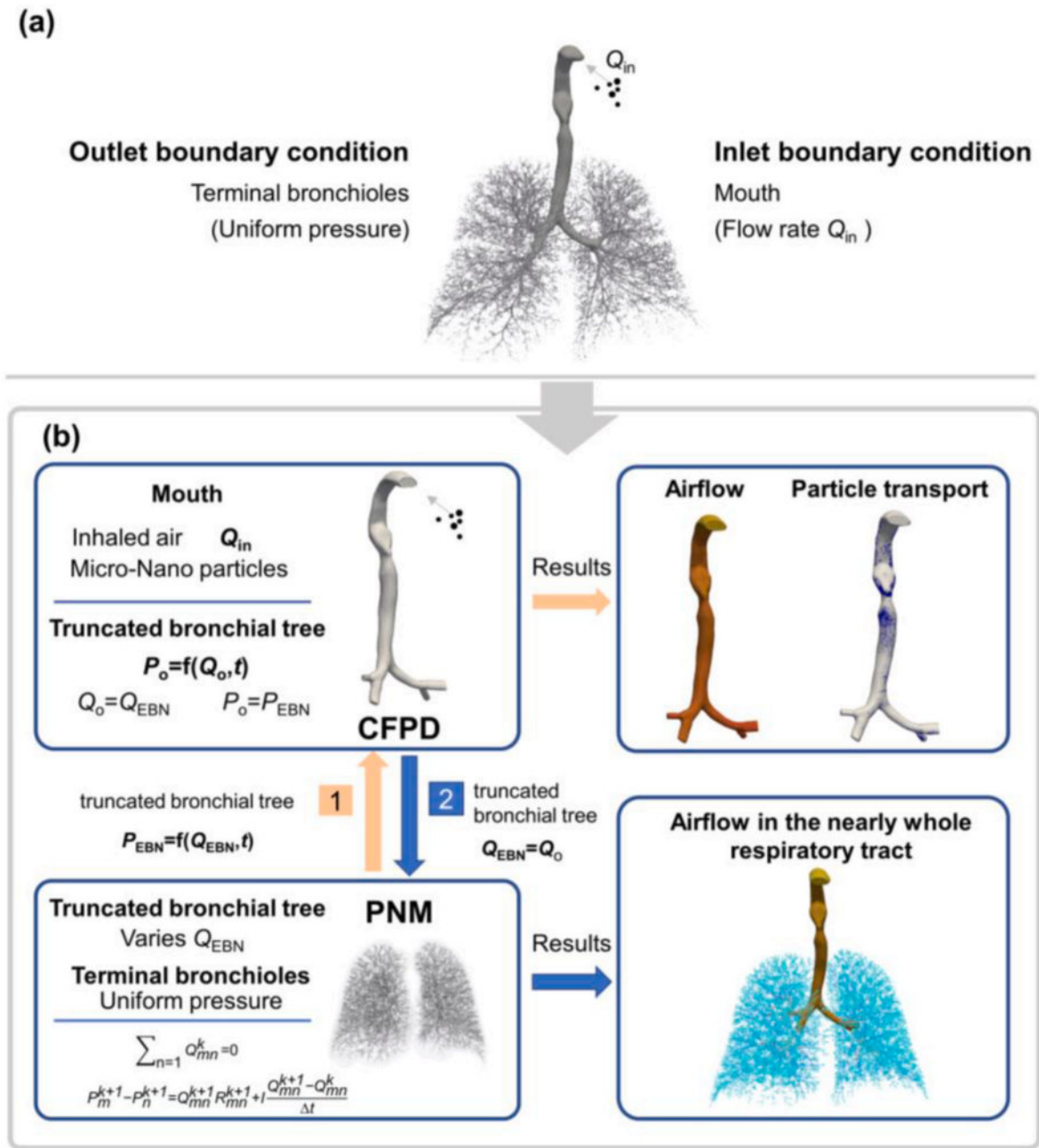


Fig. 1. Overview of EBN method: (a) Global boundary condition for the multi-scale simulation of a mouth-to-terminal bronchioles model (b) Details in CFPD of a mouth-to-truncated bronchial tree model and network model of the bronchial tree.

(LUL) and left lower lobe (LLL) are in Fig. 2(a).

2.3. Pore network model of a bronchial tree

The pore network model is utilized to simulate airflow within the bronchial tree, offering a computationally efficient alternative to CFD. In a typical pore network, the larger void space of a porous media is represented as regular pores connected by narrower throats [31]. The primary steps in the network modeling involve constructing a pore network and the subsequent modeling of the transport processes within it. Although the core concept of the pore network model is similar to the impedance network, it may offer greater accuracy than the commonly used impedance network method in biology, particularly for the airway where local cross-sectional areas vary significantly, such as diseased airways. Because the network is divided into pores and throats in the

networking modeling, which are extracted using techniques like the watershed segmentation method and the Local Hydraulic Resistance Equivalence method [32].

Due to the morphology feature of the bronchial tree, branching points are represented as zero-volume pores, while straight sections are modeled as throats that occupy the entire volume within the pore network. Furthermore, considering that Reynolds number ($Re = \frac{U D_i}{\nu}$) within airway can exceed 1600 and lead to the generation of secondary flows in the branches [33], airflow within the airway is modeled using a modified impedance approach based on Poiseuille flow [34]. It is reasonable to assume that airflow in the bronchial tree is quasi-static during low-frequency or steady-state respiration [30]. However, at high-frequency respiration, the flow model for the bronchial tree must incorporate flow inductance to account for the phase difference between flow rate and pressure wave [35–37]. This study investigates airflow in

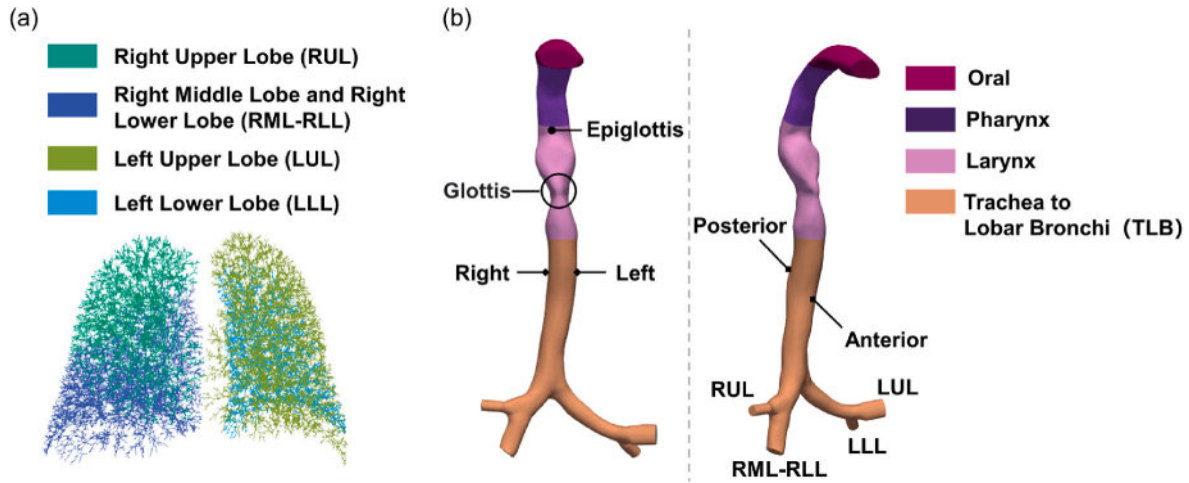


Fig. 2. View of respiratory tract models: (a) Bronchial tree model (b) Mouth-to-lobar bronchi model.

the bronchial tree during steady inhalation. The pore network model for the airway is structured as follows:

$$\sum_{n=1} Q_{mn} = 0, \quad (1)$$

$$P_m - P_n = Q_{mn} R_{mn}, \quad (2)$$

$$R_{mn} = \begin{cases} \gamma \left(Re \frac{D_t}{L} \right)^{1/2} R_{PO}, & R \geq R_{PO} \\ R_{PO}, & R < R_{PO} \end{cases}, \quad (3)$$

$$R_{PO} = \frac{128\mu L}{\pi D_t^4}, Re = \frac{UD_t}{\nu}, \quad (4)$$

where γ is the correlation coefficient of Poiseuille flow, determined by bronchial generation. Subscript ' m, n ' is pore identifier. Subscript 'PO' is the Poiseuille flow. L is the length of the throat. R is the flow resistance. μ is the dynamic viscosity. D_t is the diameter of the throat. U is the average velocity of the throat. ν is the kinematic viscosity.

To obtain the EBN boundary condition for the CFPD in the mouth-to-truncated bronchi model, the network modeling of the bronchial tree is used to determine the corresponding pressure for various flow rates at the truncated branch, assuming equal pressure at the terminal bronchi. The absolute pressure is not critical to the flow field; rather, the pressure drop is the key factor. Therefore, for simplicity, the pressure at the terminal bronchioles is set to zero in this study. This process is implemented in CHASTE package. The relationship between the pressure and flow rate at the truncation is fitted accordingly. In this study, to enhance the accuracy of the fitting, the flow rates used for fitting are approximately one order of magnitude smaller than the minimum lung lobe airflow. Therefore, corresponding pressures for 200 evenly distributed flow rates, ranging from 0 to 0.0008 m³/s at the truncated branch, are calculated, with the airflow rate in this study falling within this range. A polynomial is employed for fitting, with the resulting correlations presented in Equations (5)–(9). The corresponding fit plots are provided in Fig. S1.

$$P_{LLL} = 2.656Q_{nor}^4 - 9.569Q_{nor}^3 + 76.45Q_{nor}^2 + 541.8Q_{nor} + 629.7, \quad (5)$$

$$P_{LUL} = 2.403Q_{nor}^4 - 9.35Q_{nor}^3 + 76.62Q_{nor}^2 + 539.7Q_{nor} + 630, \quad (6)$$

$$P_{RUL} = 3.094Q_{nor}^4 - 12.03Q_{nor}^3 + 97.53Q_{nor}^2 + 681.8Q_{nor} + 792.1, \quad (7)$$

$$P_{RML-RLL} = 1.527Q_{nor}^4 - 5.874Q_{nor}^3 + 50.49Q_{nor}^2 + 359.2Q_{nor} + 423.1, \quad (8)$$

$$Q_{nor} = \frac{Q-4 \times 10^{-4}}{2.327 \times 10^{-4}}, \quad (9)$$

where the subscripts 'LLL', 'LUL', 'RUL', 'RML-RLL' represent the lung lobes corresponding to the truncated bronchi. 'nor' represent the normalized flow rate using Z-score normalization method. Q represents the flow rate entering the lobe.

2.4. CFPD of mouth-to-truncated bronchi model

2.4.1. Airflow in the model

As a result of the complex structure of airflow in a mouth-to-lobar bronchi model, CFPD is adopted to simulate the airflow under some assumptions: The air is incompressible and gas temperature is constant, as well as humidity. The respiratory tract walls are considered rigid. Inlet boundary condition is flow rate and no-slip boundary condition on the wall. Individuals inhale air at the temperature of 295 K at flow rates of 15 L per minute (LPM) (inlet $Re = 1087$), 60 LPM (inlet $Re = 4350$) and 90 LPM (inlet $Re = 7293$), corresponding to normal breath, exercise, and vigorous exercise states, respectively, as well as the different inhalation volume required for inhalation therapy [38,39]. The density of air at room temperature is 1.1967 kg/m³ and the kinematic viscosity ν is 1.532x10⁻⁵ m²/s. A transient algorithm, PIMPLE is employed to solve the pressure-velocity coupling in the Navier-Stokes equations utilizing an open-source software, OpenFOAM8® [40]. Based on this platform, nanoFoam, a custom solver is developed to produce the CFPD simulation of nano particles or larger size particles, which can be used for simulating the Brownian motion of particles at a specified temperature without solving the energy equation. A self-coded pressure-flow rate coupled boundary condition is implemented to achieve the EBN boundary condition and the schematic of the coupling algorithm is in Fig. S2. The general process is updating the pressure boundary condition at the outlet during the time marching to satisfy the correlation between the pressure P_{EBN} and the volume flow rate Q_{EBN} .

The turbulence model Shear Stress Transport (SST) $k-\omega$ is employed since it has been found that well predictive capability in transitional, turbulent flows and particle transport in oral-to-trachea model [41]. The Reynolds averaged Navier–Stokes (RANS) equations with eddy viscosity model are as follows:

$$\frac{\partial \bar{u}_i}{\partial x_i} = 0 \quad (10)$$

$$\frac{\partial \bar{u}_i}{\partial t} + \bar{u}_j \frac{\partial \bar{u}_i}{\partial x_j} = -\frac{1}{\rho} \frac{\partial \bar{p}}{\partial x_i} + \frac{\partial}{\partial x_j} \left[(\nu + \nu_t) \left(\frac{\partial \bar{u}_j}{\partial x_i} + \frac{\partial \bar{u}_i}{\partial x_j} \right) - \frac{2}{3} k \delta_{ij} \right] \quad (11)$$

where \bar{u} represents the mean velocity, ν_t is turbulence viscosity. ν is kinematic viscosity. ρ is the fluid density. k is average kinetic energy. δ_{ij} is the Kronecker delta.

The governing equation of turbulence specific dissipation rate equation, turbulence kinetic energy and other sub-models are given in the works of Menter et al. [42]. The convective term is discretized using a second-order scheme and Euler implicit time scheme is used for time discretization. Time steps for the simulation are 5×10^{-6} s, 7×10^{-6} s, 2×10^{-5} s for 90 LPM, 60 LPM and 15 LPM, respectively, and the max Courant number is in the range of 0.5 and 1. The flow field solution is considered to be converged when the mass and momentum residuals less than 10^{-4} and does not vary with further iterations.

Mesh has a significant impact on the convergence and accuracy of CFPD. The computational grid contains tetrahedral mesh within the model and 6 layers of prism mesh near the wall with the first layer height of 0.12 mm to ensure max non-dimensional wall distance $y^+ < 1$, which is 0.6 for the highest inhalation volume rate (90 LPM) in the simulation. The element size of the tetrahedral mesh is 1.15 mm and with refinements applied in regions where the flow field is complex or the average velocity is relatively high, as illustrated in Fig. 3(a). The grid size is reduced to 0.5 to 0.7 times the size of the volume mesh in the regions with the smallest cross-sectional areas of the larynx and pharynx [43–45], as well as near the tracheal carina and bronchial bifurcations [46]. The mesh for EBN method and UP method is the same. A grid independence test is conducted by monitoring the average pressure (Fig. 3(b)) and the velocity profile (Fig. 3(c)) at the glottis cross-section A-A', where the Reynolds number is relatively high and vortices are present. This test is performed at an inhalation volume of 60 LPM, with five mesh size. The mesh with 874 thousand cells is used to strike a balance computational cost and accuracy. As shown in Fig. 3(b), the relative difference is less than 1 %, and the trend falls within the plateau region for the mesh with 874 thousand cells. In Fig. 3(c), the velocity magnitude at the cross-section is nondimensionalized using the inlet velocity magnitude. The velocity profile of the 874 thousand-cell mesh

closely aligns with that of the finest mesh, except for a slightly lower peak velocity, with a relative difference of 6 %.

2.4.2. Particles transport in the model

The focus of this article is on situations where the concentration of micro and nano aerosols with particle diameter more than 0.1 μm inhaled by the human body is relatively low. Euler-Lagrange method is more suitable for this situation than Euler-Euler method [47] and spherical particles are assumed to be rigid, inertia with uniform density and diameter. Influence of particles on the flow and their collision are ignored owing to dilute aerosol. The sticky wall boundary condition is applied for particles due to mucus on the wall of the respiratory tract. The escape boundary condition of particles is used for both the inlet and outlet of the model. Additionally, uniformly distributed stationary particles are injected at the face close to the inlet, as shown in Fig. 3(d). For nano-micro particles in the respiratory tract, drag force, buoyant force, and Brownian force are the predominant forces governing particle motion [48]. The motion equations of particles are given as follows:

$$\frac{dx_i^p}{dt} = u_i^p, \quad (12)$$

$$m_p \frac{du_i^p}{dt} = F_i^D + F_i^G + F_i^{BM}, \quad (13)$$

where m_p is the mass of particle. In superscripts and subscripts, 'p' represents particles, while 'f' represents fluid. u_i^p is the component of the velocity of particle. Drag force F_i^D is calculated as [49]:

$$F_i^D = m_p \frac{3\mu C_D \text{Re}_p}{4\rho_p d_p^2 C_C} (u_i^f - u_i^p), \quad (14)$$

$$\text{Re}_p = \frac{\rho_f d_p |u_i^f - u_i^p|}{\mu}, \quad (15)$$

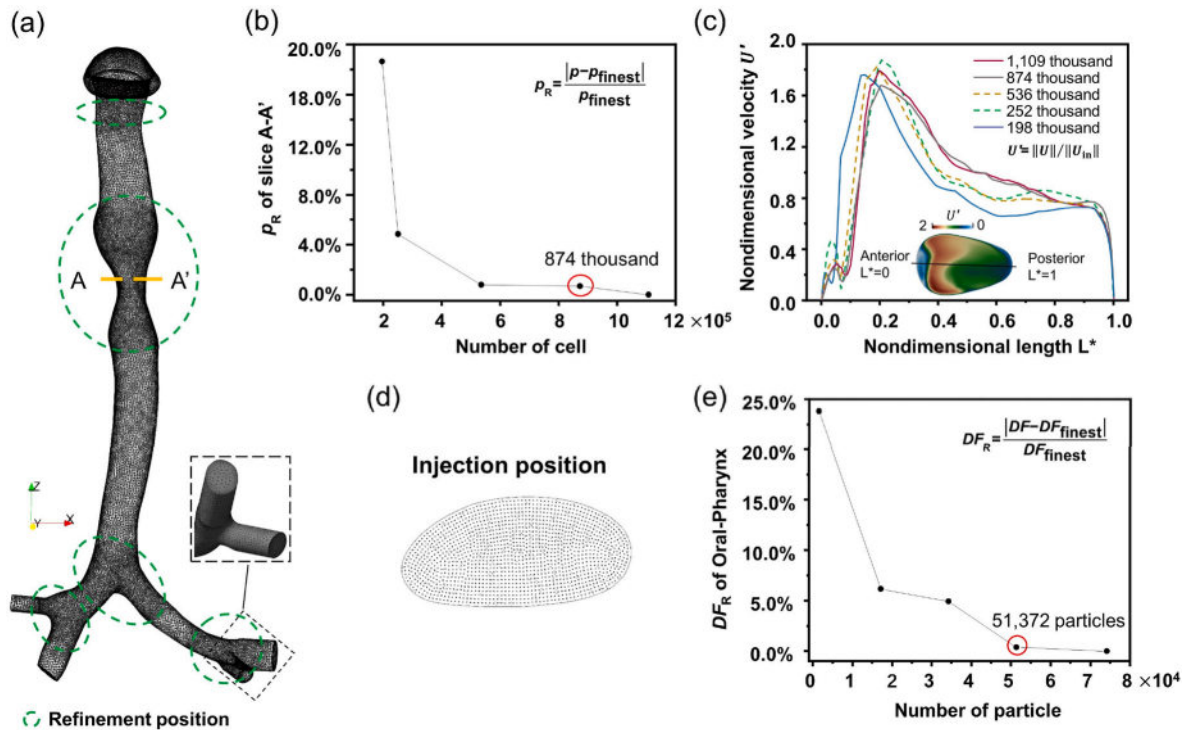


Fig. 3. The mesh of CFPD simulation and the properties of particle injection. (a) Mesh of the mouth-to-lobar bronchi model (b)The trend of the relative average pressure at cross-section A-A' with the variation of the cell number (c) Non-dimensional velocity profiles at cross-section A-A' for different mesh quantities. (d) Injection location of particles (e) Particle amount independence test.

where C_D is the drag coefficient. ρ_p is the density of the particle. Re_p is the Reynolds number of particle. d_p is the diameter of particle. Cunningham coefficient $C_c = 1 + \frac{2\lambda}{d_p} [1.257 + 0.4 \exp(-1.1(d_p/2\lambda))]$. In the room temperature, mean free path of molecule λ is 6.55×10^{-8} m.

Buoyant force F_i^G is calculated as:

$$F_i^G = m_p g_i \left(1 + \frac{\rho_f}{\rho_p} \right), \quad (16)$$

where g_i is the gravitational vector.

Brownian force can be expressed [50]:

$$F_i^{BM} = m_p G_i \sqrt{\frac{\pi S_{nm}}{\Delta t_p}}, \quad (17)$$

where $S_{nm} = \frac{2k_b T \beta m_p}{\pi m_p^2}$ is a spectral intensity function directly related to the diffusion coefficient $D_m = \frac{k_b T}{\beta m_p}$. Δt_p is the time step for particle integration, which should be less than the momentum relaxation time $\beta = \frac{3\pi \mu d_p}{m_p C_c}$. G_i is a zero-mean variant from a Gaussian probability density function. k_b is the Boltzmann constant, about 1.38×10^{-23} J/k. T is the temperature of fluid.

To account for the turbulence effect on particles, an eddy interaction model is utilized [51]. This model assumes eddy velocity $u'_i = G v_{rms}$ in the turbulence. While v_{rms} is the root mean square (RMS) of the fluid isotropic fluctuating velocity.

Deposition fraction (DF) and penetration fraction (PF) indicates the deposition probability of inhaled particles and the probability of particles passing through the region, respectively. Deposition efficiency (DE) is the ratio of DF and PF , expressed as:

$$DF = \frac{N_{dep}}{N_{mouth}}, \quad (18)$$

$$PF = \frac{N_{PF}}{N_{mouth}}, \quad (19)$$

$$DE = \frac{N_{dep}}{N_{PF}}, \quad (20)$$

$$PF_{RD} = \frac{|PF_{EBN} - PF_{UP}|}{PF_{EBN}} \times 100\%, \quad (21)$$

$$DF_{RD} = \frac{|DF_{EBN} - DF_{UP}|}{DF_{EBN}} \times 100\%, \quad (22)$$

where N_{dep} is the number of deposited particles in a specific region, N_{mouth} is the number of particles enter the mouth, N_{PF} is the number of penetrated particles into a specific region, PF_{RD} is the relative disparity of PF using EBN method and UP method, DF_{RD} is the relative disparity of DF using EBN method and UP method.

In the study, the particle diameter ranges from 0.1 to 10 μm , with a density of 5 g/cm^3 . Monte Carlo method is employed to predict the probability of particle deposition or penetration. As a result, a large number of particles are injected. To mitigate the uncertainty arising from a small number of particles, a particle independence test is conducted with 0.5 μm particle and the inhalation volume of 60 LPM. Relative deposition fraction in the oral is considered as the criterion. The result is depicted in Fig. 3(e). 51,372 particles can effectively reduce the uncertainty of the results to less than 0.5 % and ensure the computational cost is affordable.

2.5. Validation

Two cases are employed to validate the solver nanoFoam. The first case is the simulation of particle diffusing in air. The Mean Squared Displacement (MSD) of the particles is calculated and is compared with

Einstein-Stokes theory [52]. In this benchmark, particles are driven by drag force and Brownian motion. MSD of particle ($MSD_i = \langle x_i^2 \rangle - \langle x_i \rangle^2$) is compared with Einstein-Stokes theory $MSD_{ref} = 2tD_m$ and the results of 10 nm and 10 μm particles are shown in Fig. 4(a) and (b), respectively. Furthermore, the benchmark for 100 nm and 1 μm particles are shown in Fig. S3. The results indicate that the simulation results are consistent with the theory. The second one is advection and diffusion of particles through the pipe with a bend [53]. In this benchmark, 7–12 nm particles are subjected to drag force, buoyant force and Brownian force. The experimental and simulated results, $\eta_{R,sys}$, ratio of PF in the pipe with a bend and in a straight pipe are compared in Fig. 4(c). The simulation results are within the experimental error range, demonstrating that nanoFoam solver is reliable.

To validate the physiological rationality of the EBN method and the respiratory tract model, the relationship between pressure drop and flow rate between the mouth and alveoli is compared with physiological data [54,55], shown in Fig. 5(a). The ratio of pressure drop and flow represents airway resistance, which contains flow resistance and lung-deformation resistance. Flow resistance starts to play a significant role in ventilation distribution when the respiration rate increases [23]. In the pore network model, lung-deformation resistance is ignored. Nevertheless, results in Fig. 5(a) show that the relationship between pressure drop and inhalation obtained by EBN method is in the physiological range. The network model is reliable and the respiratory tract model is rational.

Moreover, the distribution of flow rate in lobes is simulated using EBN method and UP method, separately. Results are compared with data from literature [56,57], shown in Fig. 5(b). The distribution acquired by EBN method is consistent with physiological data at rest or exercise situations, while the results of UP method deviate from the data. This indicates that EBN method is more accurate and closer to the reality in predicting airflow distribution compared to the UP method.

To validate CFPD simulation in this study, the deposition fraction in oral is compared with vivo experimental [58] and vitro experimental data [59,60], as shown in Fig. 5(c). Results are agreed with the experimental data and CFPD simulation in the mouth-to-lobar bronchi model is reliable.

3. Results and discussion

3.1. Comparison between EBN and UP methods

EBN modeling process can provide flow field information in the nearly whole respiratory tract model at specific inhalation volume, as illustrated in the overview (Fig. 1). The pressure from mouth to alveoli and the distribution of Reynolds number of airways in the bronchial tree is provided in Fig. S4. However, UP method is unable to simulate the flow in the high-generation bronchioles. Furthermore, the distribution of flow rate in lobes varies significantly using two methods as shown in Table 1. The maximum difference in flow rate distribution is in the RML-RLL, which is about 20 %. Moreover, the flow rate in RUL is the smallest using EBN method while in UP method, the smallest flow rate is in LLL. Flow rate distribution in lobes in EBN method is more uniform than UP method.

Due to the complex structure of the respiratory tract and high Re , the airflow in the model generates numerous vortices, which could have an impact on particle transport. Therefore, the contour of Q criterion is employed to visualize the vortex structure in Fig. 6(a), when Q criterion $>100,000$ at the flow rate of 60 LPM and Q criterion >2500 at the flow rate of 15 LPM. For the inhalation volume of 60 LPM, there is a slight difference in the vortex below the glottis and within the bronchi between UP and EBN method. For the inhalation volume of 15 LPM, variations in vortex structures are obvious from the larynx to the bronchi, particularly in the trachea. The EBN method depicts a vortex beam in the lower half of the trachea which is absent in the results of UP method.

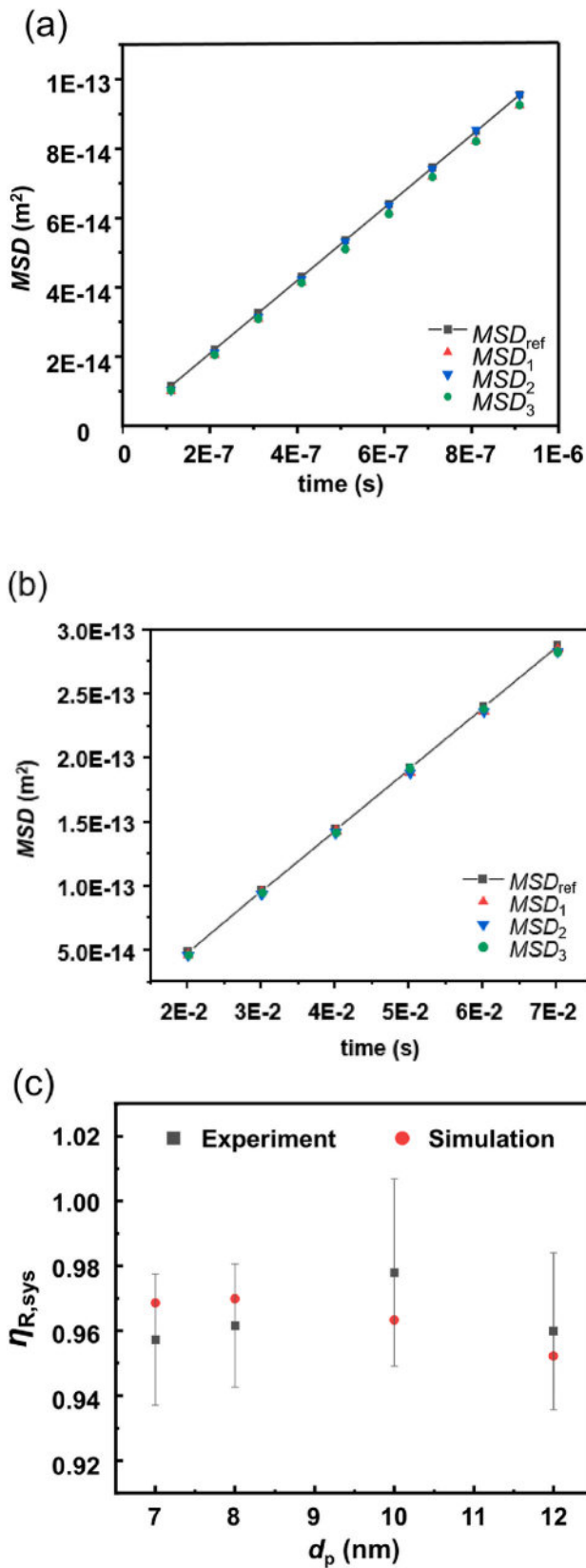


Fig. 4. Benchmarks of nanoFoam solver: (a) MSD of 10 nm particles undergoing free diffusion in air which are compared with the Einstein-Stokes theory. (b) MSD of 10 μm particles undergoing free diffusion in air, which are compared with the Einstein-Stokes theory. (c) Comparison of the ratio of penetration fraction in the pipe with a bend and in a straight pipe.

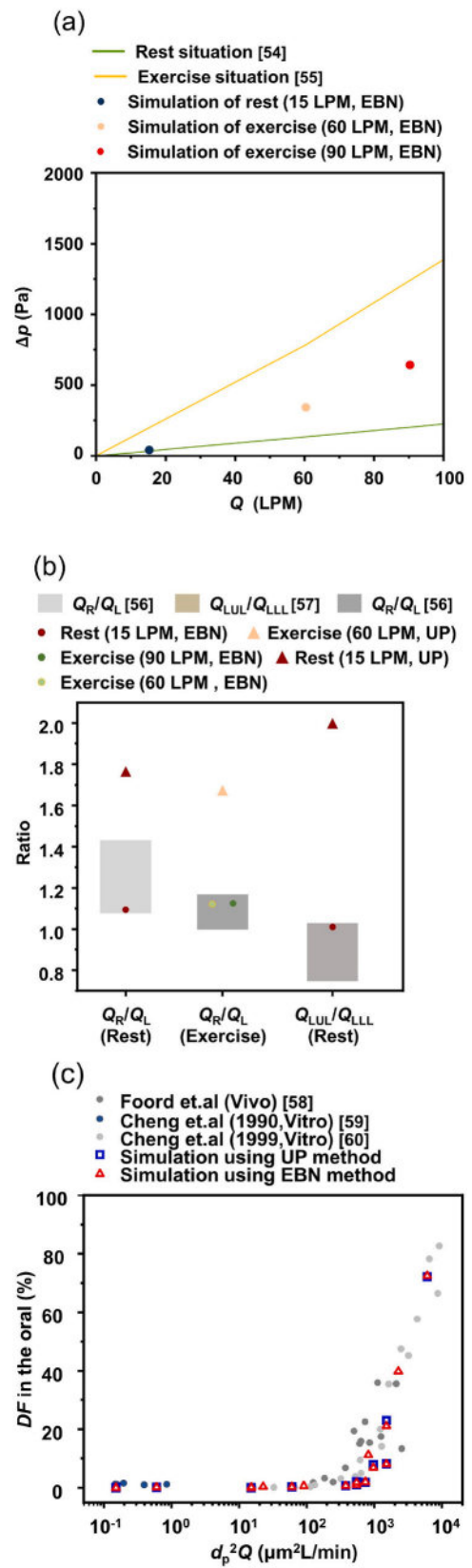


Fig. 5. Validation of airflow and particle deposition: (a) Comparison of the relationship between pressure drop and flow in mouth-to-terminal bronchioles. (b) Comparison of volume flow rate distribution in lobes. (c) Comparison of DF in oral.

Table 1

The proportion of airflow distribution in different lung lobes with the EBN and UP methods.

	$Q_{in} = 15 \text{ LPM}$				$Q_{in} = 60 \text{ LPM}$			
	Q_{LLL}	Q_{LUL}	Q_{RUL}	$Q_{RML-RLL}$	Q_{LLL}	Q_{LUL}	Q_{RUL}	$Q_{RML-RLL}$
EBN	24.2	23.6	20.0	32.2	23.5	23.7	20.3	32.5
	%	%	%	%	%	%	%	%
UP	12.0	24.0	12.2	51.8	10.3	27.0	12.7	50.0
	%	%	%	%	%	%	%	%

These disparities in airflow field structures will lead to the difference in the particle transport between two methods.

In this study, the relative disparity of penetration fraction (PF_{RD}) and deposition fraction (DF_{RD}) defined in Eq.(21) and (22) are used to quantify the differences in particle deposition and penetration rates between two methods. As Fig. 6(b) shows, the relative disparity of PF in the right lung exhibits the greatest difference between the methods when inhaling particles ranging from 0.1 to 7 μm at the flow rate of 15

LPM, while PF_{RD} in the left lung has the greatest difference when inhaling particles ranging from 0.1 to 3 μm at the flow rate of 60 LPM. Specifically, the maximum disparity of 93 % occurs in the RML-RLL when 7 μm particles are inhaled at the flow rate of 15 LPM. This indicates that two methods have significant differences in predicting particle penetration rates in lobes. Fig. 6(c) illustrates the relative disparity of DF in two methods. The maximum DF_{RD} in the truncated model is 6 % when inhaling 7 μm particles at a flow rate of 15 LPM. In the pharynx and larynx, the DF_{RD} is relatively small. However, in the TLB region, the disparity between two methods is the highest, due to discrepancies in airflow vortex structures in the TLB using two methods. Specifically, when inhaling 5 μm particles at the flow rate of 60 LPM, there is a maximum DF_{RD} of 30 %.

3.2. Deposition and penetration fraction

This paper reveals the particle transport in the mouth-to-lobar bronchi model with EBN method. Fig. 7(a-c) shows the particle deposition in each part of the mouth-to-lobar bronchi model. In the model, the probability of particle deposition in the upper respiratory tract

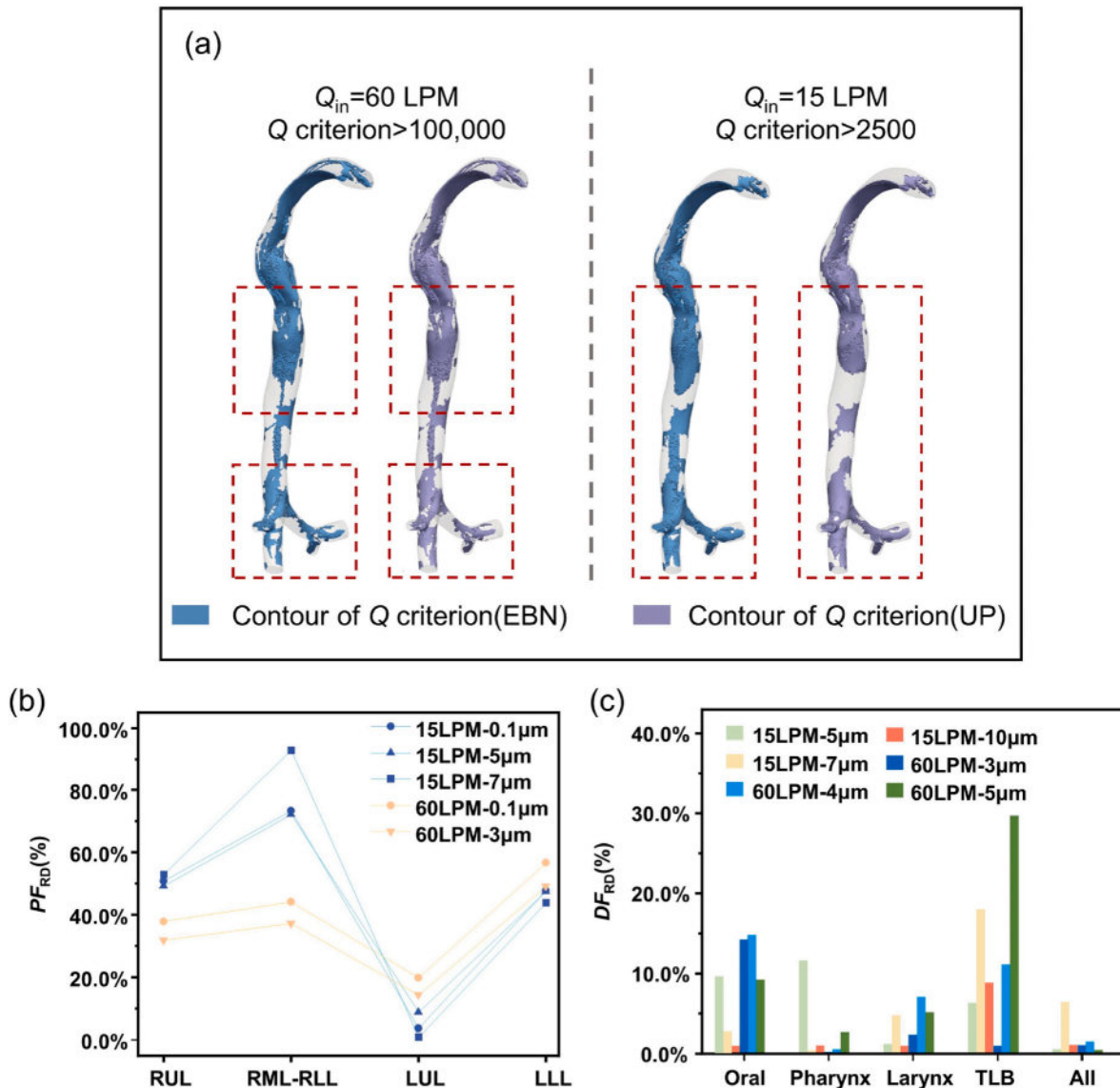


Fig. 6. Comparison of CFPD simulation results using the UP and EBN methods on the mouth-to-lobar bronchi model: (a) Comparison of vortex structures in the mouth-to-lobar bronchi model using two methods. (b) Relative disparity of PF at different inhalation volumes. (c) The relative disparity of DF at different inhalation volumes.

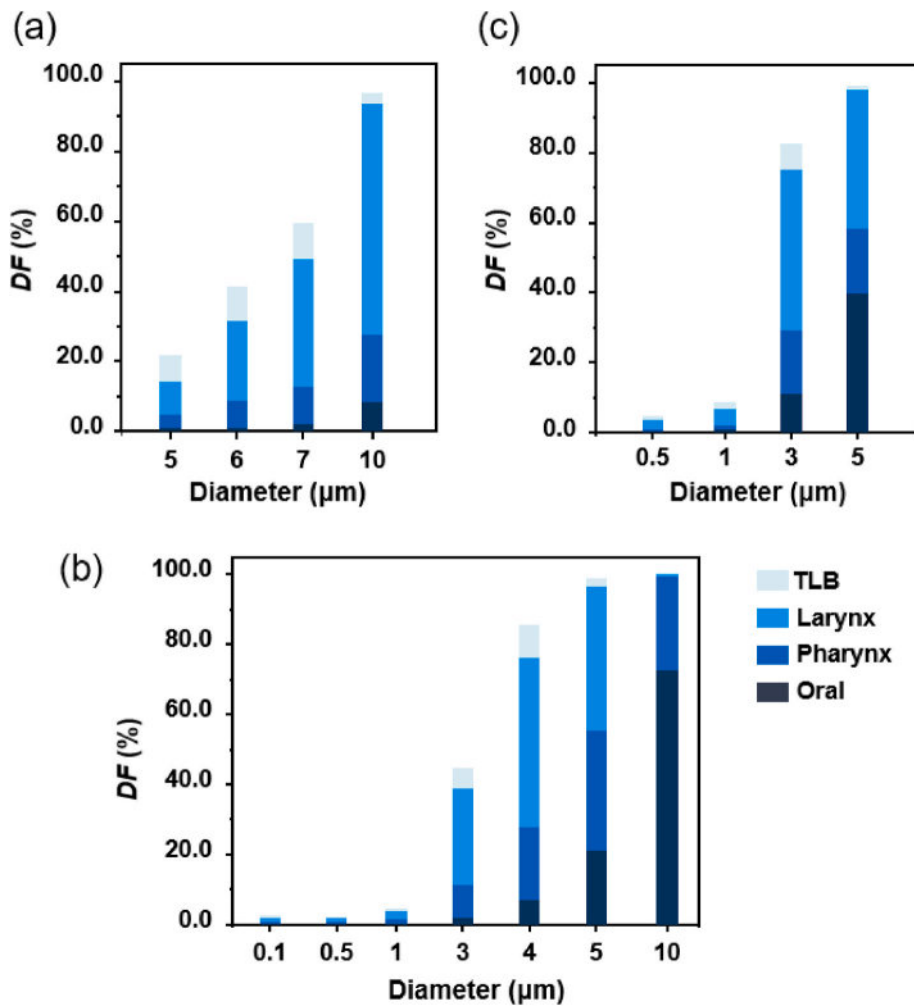


Fig. 7. Deposition fraction of particles in different segments of the mouth-to-lobar bronchi model: (a) $Q_{in} = 15$ LPM (b) $Q_{in} = 60$ LPM(c) $Q_{in} = 90$ LPM.

increases with the larger size of micron particles and higher flow rates. For the same size particles (i.e. $d_p = 5 \mu\text{m}$), DF of the model increases with higher inhalation volume. Most of the inhaled 5–10 μm particles deposit in the larynx when they are inhaled at the flow rate of 15 LPM. While at the inhalation of 60, 90 LPM, the most likely deposition region shifts from the larynx to the oral-pharynx with the increase of particle size. In addition, when particles with the diameter more than 6 μm are inhaled at the flow rate of 15 LPM or more than 3 μm are inhaled at the flow rate of 60 LPM, particles will deposit in the model with a likelihood of 40%. DF in the model is more than 80% for particles with diameter larger than 3 μm inhaled at the flow rate of 90 LPM. Therefore, when designing inhalation drugs for the treatment of lung diseases, it's preferable for the particle size to be less than 3 μm with the inhalation volume ranges from 15 to 90 LPM. Furthermore, pollutants with size larger than 3 μm are more likely to deposit in the upper respiratory tract, then be removed to the mouth and cause less harm.

The probability of particles penetrating into different lobes from lobar bronchi is shown in Fig. 8(a–c). When 0.1 ~ 1 μm particles are inhaled, flow rate and particle size have little impact on PF and more than 90% particles will penetrate deeper into the lung lobes, while PF will be more than 95% at the rate of 15 or 60 LPM. For microparticles ($d_p \geq 1 \mu\text{m}$), PF decreases with the increase of particle size and flow rate, in contrast to the trend of DF . When $PF > 20\%$, the probability of particles entering RML-RLL is the highest among lobes, while PF of RUL and RML-RLL bronchi will be comparable when $PF < 20\%$. Hence, when designing inhalation medications for the treatment of lung diseases, particles should ideally have a diameter ranging from 0.1 to 1 μm

and be inhaled at the flow rate of 15 or 60 LPM. However, this also indicates that when 0.1 and 1 μm pollutant particles are inhaled, they are highly likely to transport deep into the lungs, potentially causing lung diseases.

3.3. Deposition hotspot and deposition mechanism

Deposition mechanisms of the particle in the respiratory tract include diffusion deposition, gravitational deposition and inertial deposition. Gravitational deposition typically plays a role in small bronchi and alveoli. Additionally, Peclet number Pe indicates that diffusion deposition can be neglected when 0.1–10 μm particles deposit on the wall of the truncated respiratory tract model. Peclet number $Pe = \frac{UD_m}{D_m}$ at inlet is more than the magnitude of $1e7$ in this study, where characteristic length D is the hydraulic diameter of the mouth, U is the average velocity at the mouth. Subsequently, the inlet Reynolds number and Stokes number ($Stk = \frac{\rho_p d_p^2 Cc U}{18\mu D_m}$) are used to be the characteristic number of the airflow and inertia deposition of particles, respectively. Deposition efficiency (DE) is used to characterize the particle deposition probability in each part.

The variation of DE concerning Stk and Re in the truncated respiratory tract model is in Fig. 9(a–c, e). The segments of the respiratory tract and corresponding observation direction of the respiratory tract are in Fig. 9(b). When $Stk < 0.01$, DE of all parts of the model is less than 10% and does not vary significantly with Stk , indicating particles can closely track the streamline of airflow. When $Stk > 0.01$, DE of particles at all

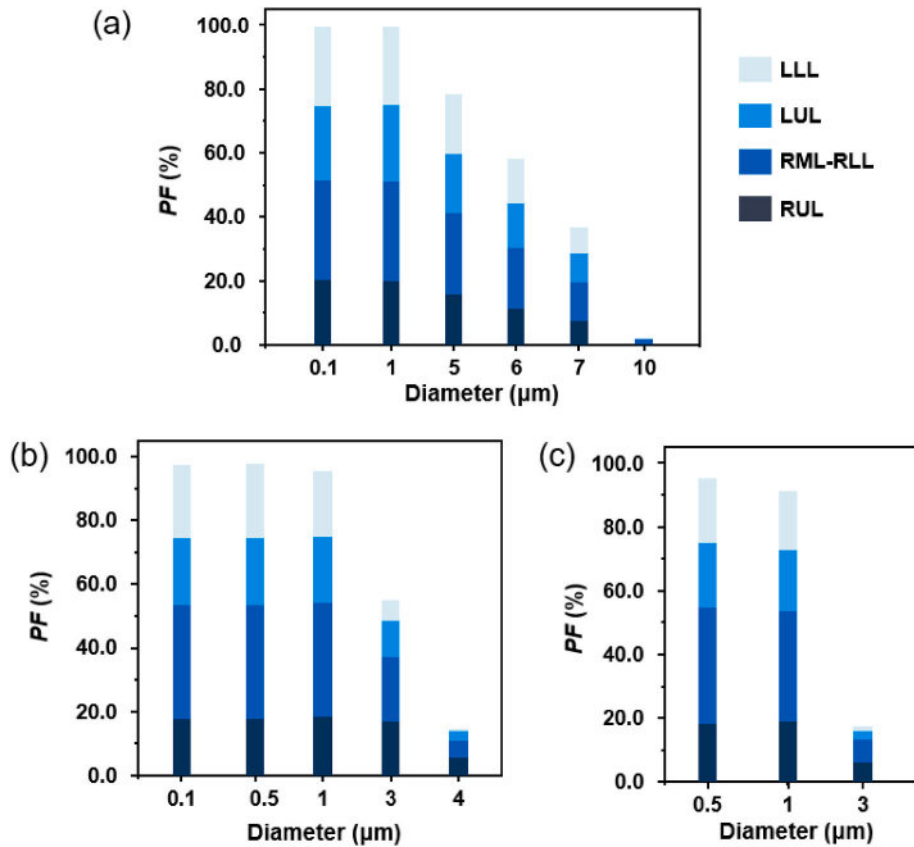


Fig. 8. Penetration fraction of particles into lobes from lobar bronchi: (a) $Q_{in} = 15$ LPM (b) $Q_{in} = 60$ LPM (c) $Q_{in} = 90$ LPM.

parts of the respiratory tract rapidly rises with the increase of Stk . In the oral-pharynx, Re significantly influences DE when $Stk > 0.01$, while minimal influence of Re on DE occurs in the larynx and TLB. Although the variation of DE might not be significant with Re and Stk , the deposition hotspots of particles change with Re and Stk .

The deposition hotspots of particles are determined by the flow structure such as vortex and jet flow, as well as the particle inertia. When Re number varies, the vortex structure in the oral-pharynx changes accordingly, leading to different deposition shapes even with the similar Stk number of particles, as shown in Fig. 9(a) (B, C, D). When $Re \sim 1000$, as depicted in Fig. 9(a), most of the deposited particles concentrate on the sidewalls and anterior wall of the pharynx (Anterior, posterior, left and right sides are regulated in Fig. 2(b)), since no vortex rope near the posterior wall of the oral-pharynx, as shown in Fig. 9(d). However, deposited particles tend to concentrate on the posterior wall of the oral-pharynx when Re is about 5000 and 7000 due to vortex ropes near the posterior wall. When $Re \sim 5000$, four vortex ropes arise near the posterior wall of the oral, with two of them extending from the mouth to the pharynx in Fig. 9(d). Thus, when Stk of particles is about 1, ribbon-like deposition forms on the posterior wall of the pharynx, with a blank stripe in the center, shown in Fig. 9(a) (A). In Fig. 9(a) (C), a deposition streak appears on the center of the posterior wall in pharynx for $Stk \sim 0.1$. When $Re \sim 7000$, two vortex ropes arise near the posterior wall of the oral and a blank deposition stripe also appears with $Stk \sim 0.2$, shown in Fig. 9(a) (B), and deposited particles with $Stk \sim 0.1$ scatter more uniformly on the posterior wall shown in Fig. 9(a) (E).

As shown in Fig. 9(c) (G), when $Stk < 0.01$, the amount of particle deposition in the larynx is small but most of the deposited particles will be concentrated around the glottis. When $Stk = 0.01-0.1$ (Fig. 9(c) (D, E, F)), there is a high probability of deposited particles scatter on the lower anterior side of the glottis, the posterior corner of the epiglottis and the sidewalls from the epiglottis to the glottis. As $Stk > 0.2$ (Fig. 9(c) (B)), the

deposition hotspot is a narrow streak extending from the pharynx to the posterior corner of the epiglottis, as well as the deposition below the glottis in larynx. When $Stk \sim 1$, the deposited particles below the glottis diminishes greatly (Fig. 9(c) (A)). The deposition in the sidewall of epiglottis to the glottis is also mainly influenced by the vortex in the larynx, as illustrated in Fig. 9(f). In Fig. 9(f), a local low-speed region closing to the anterior of the epiglottis-glottis area, suggests the presence of vortex, which is also shown in Fig. 6(c). Moreover, inertia particles deposited around the posterior corner of the epiglottis and around the glottis are affected by the abrupt change of airflow direction near the corner, shown in Fig. 9(f). The high-velocity jet flow near the lower anterior posterior wall of the glottis enhances the deposition.

In TMB, as shown in Fig. 9(e), DE is primarily influenced by Stk . Few of particles with $Stk > 0.1$ (Fig. 9(e) (A, B)) enter the TLB region and over 60 % of them will deposit on the upper half wall of the trachea. More particles with $Stk = 0.01-0.1$ (Fig. 9(e) (C, D, E)) enter the trachea and deposit in the upper half wall of the trachea, at the junction of branches as well as on the outer curved side of bronchi. Most of the particles with $Stk < 0.01$ enter the lobes (Fig. 9(e) (C, D)). Particle deposition in the trachea is primarily affected by the laryngeal jet flow in Fig. 9(f) and the laryngeal vortex extending to the trachea in Fig. 9(d). Moreover, inertial particles deposit at the junction of bronchi for sudden change in fluid direction, and the inertial particles move towards the outer curved side wall as the centrifugal force on the airflow in bronchi.

3.4. Discussion

The EBN method for particle transport in the mouth-to-truncated bronchial tree model has broad applicability across both idealized and image-based models. Additionally, this method can be applied to simulate breath with respiratory waveform and avoid manually transferring the data of the flow field between 1D and 3D simulation at the

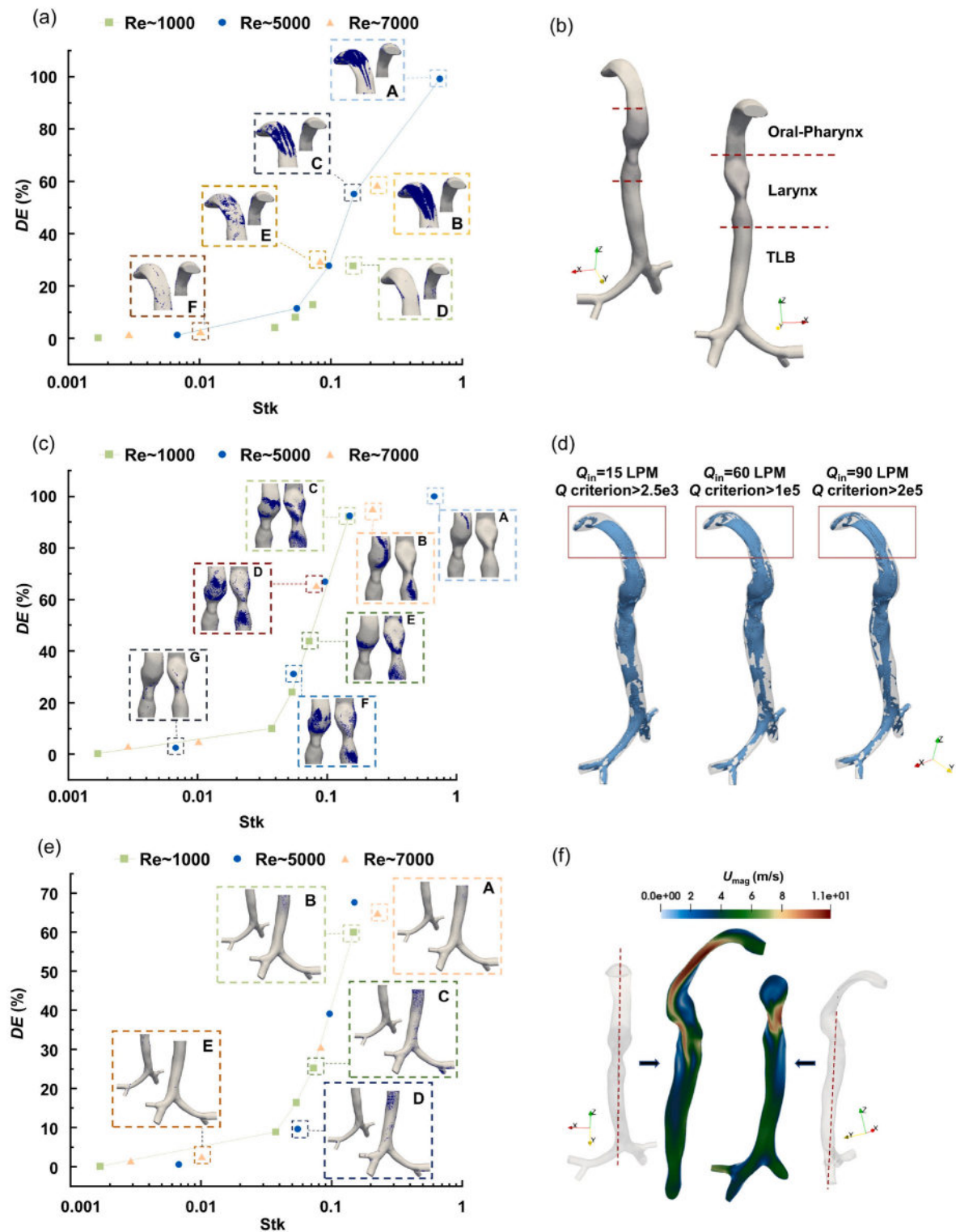


Fig. 9. Particle deposition efficiency, deposition hotspots, and airflow (a) Particle deposition efficiency and deposition hotspots in the oral-pharynx regions (b) Corresponding orientation of the model in the deposition hotspot map, as well as the corresponding parts of the model in the deposition efficiency map (c) Particle deposition efficiency and deposition hotspots in the larynx (d) Vortex structures in the model at three inhalation volumes (e) Particle deposition efficiency and deposition hotspots in the TLB region (f) Cross-sectional velocity magnitude contour of the airflow in the model.

truncation. This study employs a transient algorithm in CFPD to simulate breath with steady waveform, indicating that the EBN method is well-suited for simulating the inspiratory process. However, certain parameters in the simulation of the breathing process, such as time steps at different scales, need to be carefully selected to ensure both the convergence of the flow field and the accuracy of the coupling

algorithm. Moreover, it is necessary to modify the pore scale model when the quasi-static assumption is no longer valid [36], such as in cases of higher respiratory rates. Additionally, EBN modeling method reveals the airflow from mouth-to-terminal bronchioles, laying the foundation for studying aerosol transport throughout the whole respiratory tract model.

Future research could improve the network model of the bronchial tree and CFPD of the mouth-to-truncated model. This study ignores the deformation of the lung, which might play a role in less inhalation flow rate. EBN method assumes equal alveolar pressure at the terminal bronchioles, while slight physiological variations may exist among them due to factors such as gravity, total lung capacity, compliance, and inhalation rate. In this paper, the results are validated, suggesting that these factors can be neglected. However, at lower inhalation rates, alveolar pressure may become a key factor influencing airflow distribution. Moreover, the results of steady-state inhalation simulations in this study may exhibit some deviations compared to those of high-frequency breathing at the equivalent inspiratory volume.

4. Conclusions

This study proposes a multi-scale modeling method for the aerosol transport in a mouth-to-truncated bronchial tree model, called EBN, which provides a more physiologically consistent boundary condition than the widely used uniform pressure boundary condition for CFPD simulation. Compared with previous studies on multi-scale simulation of airflow in the whole respiratory tract, the coupling algorithm between scales is more readily implementable and flexible with EBN boundary condition. Moreover, this method is suitable for both image-based and idealized respiratory tract model. It can also be applied to simulate breathing with a respiratory waveform.

A comparison between EBN method and UP method is presented. The results indicate that the maximum difference between these two methods in flow distribution of lobes is about 20 %. The maximum relative disparity of aerosol penetration fraction of the RML-RLL lobes is 93 % when inhaling 7 μm particles at the flow rate of 15 LPM. Furthermore, the maximum relative disparity of aerosol deposition fraction within the TLB is 30 % when inhaling 5 μm particles at the flow rate of 60 LPM.

Results of the simulation of the nano-micro particles transport in the mouth-to-lobar bronchi model using EBN method show that: Particles for drug delivery into the lung should ideally have a diameter ranging from 0.1 to 1 μm and be inhaled at the flow rate ranging from 15 to 60 LPM. However, these particles will be harmful if get inhaled as pollutants. Meanwhile, particle deposition fraction and deposition efficiency at each part of the truncated model are revealed. This paper also qualitatively analyzes deposition hotspots forming reason corresponding to inlet Stk and Re. The dominating deposition mechanism of 0.1–10 μm particle of 5 g/m^3 inhaled at the flow rate of 15–90 LPM is inertia deposition.

This work provides a reference for the optimization of drug delivery, targeted therapy, and the prevention and control of pollutants. It also lays a foundation for the simulation of aerosol transport in the whole respiratory tract.

CRedit authorship contribution statement

Han Xiao: Writing – original draft, Investigation. **Yang Liu:** Writing – review & editing, Validation. **Bingbing Sun:** Writing – review & editing. **Yiyang Guo:** Writing – review & editing. **Moran Wang:** Writing – review & editing, Validation, Supervision, Project administration, Conceptualization.

Declaration of competing interest

The authors declare that they have no known competing financial interests or personal relationships that could have appeared to influence the work reported in this paper.

Acknowledgements

This work is financially supported by the National Natural Science

Foundation grant of China (No. 12432013, 12272207).

Appendix A. Supplementary data

Supplementary data to this article can be found online at <https://doi.org/10.1016/j.compbiomed.2024.109292>.

References

- [1] S. Chakraborti, T. Chakraborti, S.K. Das, D. Chattopadhyay, *Oxidative Stress in Lung Diseases*, Springer, Singapore, 2019.
- [2] W.K. Jo, J.J. Seo, Indoor and outdoor bioaerosol levels at recreation facilities, elementary schools, and homes, *Chemosphere* 61 (2005) 1570–1579, <https://doi.org/10.1016/j.chemosphere.2005.04.103>.
- [3] L. Tian, Y. Shang, R. Chen, R. Bai, C. Chen, K. Inthavong, J. Tu, A combined experimental and numerical study on upper airway dosimetry of inhaled nanoparticles from an electrical discharge machine shop, *Part. Fibre Toxicol.* 14 (2017) 24, <https://doi.org/10.1186/s12989-017-0203-7>.
- [4] J.J.e. Li, S. Muralikrishnan, C.-T. Ng, L.-Y.L. Yung, B.-H. Bay, Nanoparticle-induced pulmonary toxicity, *Exp. Biol. Med.* 235 (2010) 1025–1033, <https://doi.org/10.1258/ebm.2010.010021>.
- [5] J.B. Soriano, P.J. Kendrick, K.R. Paulson, V. Gupta, E.M. Abrams, R.A. Adedoyin, T. B. Adhikari, S.M. Advani, A. Agrawal, E. Ahmadian, Prevalence and attributable health burden of chronic respiratory diseases, 1990–2017: a systematic analysis for the Global Burden of Disease Study 2017, *Lancet Respir. Med.* 8 (2020) 585–596, [https://doi.org/10.1016/S2213-2600\(20\)30105-3](https://doi.org/10.1016/S2213-2600(20)30105-3).
- [6] S. Anderson, P. Atkins, P. Bäckman, D. Cipolla, A. Clark, E. Daviskas, B. Disse, P. Entcheva-Dimitrov, R. Fuller, I. Gonda, Inhaled medicines: past, present, and future, *Pharmacol. Rev.* 74 (2022) 48–118, <https://doi.org/10.1124/pharmrev.120.000108>.
- [7] M. Sanders, Inhalation therapy: an historical review, *Prim. Care Respir. J.* 16 (2007) 71–81, <https://doi.org/10.3132/pcrj.2007.00017>.
- [8] A.V. Kolanjiyil, C. Kleinstreuer, Nanoparticle mass transfer from lung airways to systemic regions-part i: whole-lung aerosol dynamics, *J. Biomech. Eng.* 135 (2013) 121003, <https://doi.org/10.1115/1.4025332>.
- [9] V.K. Bui, J.-Y. Moon, M. Chae, D. Park, Y.-C. Lee, Prediction of aerosol deposition in the human respiratory tract via computational models: a review with recent updates, *Atmosphere* 11 (2020) 137, <https://doi.org/10.3390/atmos11020137>.
- [10] S. Guha, P. Hariharan, M.R. Myers, Enhancement of ICRP's lung deposition model for pathogenic bioaerosols, *Aerosol. Sci. Technol.* 48 (2014) 1226–1235, <https://doi.org/10.1080/02786826.2014.975334>.
- [11] V. Martins, M. Cruz Minguillón, T. Moreno, X. Querol, E. de Miguel, M. Capdevila, S. Centelles, M. Lazaridis, Deposition of aerosol particles from a subway microenvironment in the human respiratory tract, *J. Aerosol Sci.* 90 (2015) 103–113, <https://doi.org/10.1016/j.jaerosci.2015.08.008>.
- [12] K. Ahooshosh, M. Saidi, M. Mohammadpourfard, H. Aminfar, H. Hamishehkar, A. Farnoud, O. Schmid, Flow structure and particle deposition analyses for optimization of a pressurized metered dose inhaler (pMDI) in a model of tracheobronchial airway, *Eur. J. Pharmaceut. Sci.* 164 (2021) 105911, <https://doi.org/10.1016/j.ejps.2021.105911>.
- [13] K. Ahooshosh, O. Pourmehran, H. Aminfar, M. Mohammadpourfard, M. Sarafraz, H. Hamishehkar, Development of human respiratory airway models: a review, *Eur. J. Pharmaceut. Sci.* 145 (2020) 105233, <https://doi.org/10.1016/j.ejps.2020.105233>.
- [14] A.P. Kuprat, M. Jalali, T. Jan, R.A. Corley, B. Asgharian, O. Price, R.K. Singh, S. Colby, C. Darquenne, Efficient bi-directional coupling of 3D computational fluid-particle dynamics and 1D Multiple Path Particle Dosimetry lung models for multiscale modeling of aerosol dosimetry, *J. Aerosol Sci.* 151 (2021) 105647, <https://doi.org/10.1016/j.jaerosci.2020.105647>.
- [15] A.P. Kuprat, O. Price, B. Asgharian, R.K. Singh, S. Colby, K. Yugulis, R.A. Corley, C. Darquenne, Automated bidirectional coupling of multiscale models of aerosol dosimetry: validation with subject-specific deposition data, *J. Aerosol Sci.* 174 (2023) 106233, <https://doi.org/10.1016/j.jaerosci.2023.106233>.
- [16] J. Zhao, Y. Feng, M. Bezerra, J. Wang, T. Sperry, Numerical simulation of welding fume lung dosimetry, *J. Aerosol Sci.* 135 (2019) 113–129, <https://doi.org/10.1016/j.jaerosci.2019.05.006>.
- [17] N.D. Khoa, S. Li, N.L. Phuong, K. Kuga, H. Yabuuchi, O.K. Kan, K. Matsumoto, K. Ito, Computational fluid-particle dynamics modeling of ultrafine to coarse particles deposition in the human respiratory system, down to the terminal bronchiole, *Comput. Methods Progr. Biomed.* 237 (2023) 107589, <https://doi.org/10.1016/j.cmpb.2023.107589>.
- [18] Z. Zhang, C. Kleinstreuer, Airflow structures and nano-particle deposition in a human upper airway model, *J. Comput. Phys.* 198 (2004) 178–210, <https://doi.org/10.1016/j.jcp.2003.11.034>.
- [19] J. Williams, J. Kolehmainen, S. Cunningham, A. Ozel, U. Wolfram, Effect of patient inhalation profile and airway structure on drug deposition in image-based models with particle-particle interactions, *Int. J. Pharm.* 612 (2022) 121321, <https://doi.org/10.1016/j.ijpharm.2021.121321>.
- [20] A. Tiwari, A. Jain, A.R. Paul, S.C. Saha, Computational evaluation of drug delivery in human respiratory tract under realistic inhalation, *Phys. Fluids* 33 (2021) 083311, <https://doi.org/10.1063/5.0053980>.
- [21] J. Wedel, P. Steinmann, M. Štrákl, M. Hriberšek, Y. Cui, J. Ravník, Anatomy matters: the role of the subject-specific respiratory tract on aerosol deposition—a

- CFD study, *Comput. Methods Appl. Mech. Eng.* 401 (2022) 115372, <https://doi.org/10.1016/j.cma.2022.115372>.
- [22] Z. Zhang, C. Kleinstreuer, Computational analysis of airflow and nanoparticle deposition in a combined nasal–oral–tracheobronchial airway model, *J. Aerosol Sci.* 42 (2011) 174–194, <https://doi.org/10.1016/j.jaerosci.2011.01.001>.
- [23] Y.H. Chang, C.P. Yu, A model of ventilation distribution in the human lung, *Aerosol. Sci. Technol.* : J. Am. Assoc. Aerosol Res. 30 (1999) 309–319, <https://doi.org/10.1080/027868299304660>.
- [24] Y. Yin, J. Choi, E.A. Hoffman, M.H. Tawhai, C.L. Lin, A multiscale MDCT image-based breathing lung model with time-varying regional ventilation, *J. Comput. Phys.* 244 (2013) 168–192, <https://doi.org/10.1016/j.jcp.2012.12.007>.
- [25] F. Jiang, T. Hirano, C. Liang, G. Zhang, K. Matsunaga, X. Chen, Multi-scale simulations of pulmonary airflow based on a coupled 3D-1D-0D model, *Comput. Biol. Med.* 171 (2024) 108150, <https://doi.org/10.1016/j.combiomed.2024.108150>.
- [26] M.J. Blunt, *Multiphase Flow in Permeable Media: A Pore-Scale Perspective*, Cambridge university press, Cambridge, 2017.
- [27] F.R. Cooper, R.E. Baker, M.O. Bernabeu, R. Bordas, L. Bowler, A. Bueno-Orovio, H. M. Byrne, V. Carapella, L. Cardone-Noott, C. Jonatha, S. Dutta, B.D. Evans, A. G. Fletcher, J.A. Grogan, W. Guo, D.G. Harvey, M. Hendrix, D. Kay, J. Kursawe, P. K. Maini, B. McMillan, G.R. Mirams, J.M. Osborne, P. Pathmanathan, J.M. Pitt-Francis, M. Robinson, B. Rodriguez, R.J. Spiteri, D.J. Gavaghan, Chaste: cancer, Heart and Soft Tissue environment, *J. Open Source Softw.* 5 (2020) 1848, <https://doi.org/10.21105/joss.01848>.
- [28] M.H. Tawhai, A.J. Pullan, P.J. Hunter, Generation of an anatomically based three-dimensional model of the conducting airways, *Ann. Biomed. Eng.* 28 (2000) 793–802, <https://doi.org/10.1114/1.1289457>.
- [29] M.H. Tawhai, P. Hunter, J. Tschirren, J. Reinhardt, G. McLennan, E.A. Hoffman, CT-based geometry analysis and finite element models of the human and ovine bronchial tree, *J. Appl. Physiol.* 1985 (97) (2004) 2310–2321, <https://doi.org/10.1152/japplphysiol.00520.2004>.
- [30] S. Middleton, E. Dimbath, A. Pant, S.M. George, V. Maddipati, M.S. Peach, K. Yang, A.W. Ju, A. Vahdati, Towards a multi-scale computer modeling workflow for simulation of pulmonary ventilation in advanced COVID-19, *Comput. Biol. Med.* 145 (2022) 105513.
- [31] M.J. Blunt, Flow in porous media — pore-network models and multiphase flow, *Curr. Opin. Colloid Interface Sci.* 6 (2001) 197–207, [https://doi.org/10.1016/S1359-0294\(01\)00084-X](https://doi.org/10.1016/S1359-0294(01)00084-X).
- [32] Y. Liu, W. Gong, Y. Zhao, X. Jin, M. Wang, A pore-throat segmentation method based on local hydraulic resistance equivalence for pore-network modeling, *Water Resour. Res.* 58 (2022) e2022WR033142, <https://doi.org/10.1029/2022WR033142>.
- [33] K. Pradhan, A. Guha, P.K. Halder, Characteristics of pressure drop, mass flow distribution and flow asymmetry in three-dimensional branching networks based on model human bronchial tree, *ZAMM Z. Angew. Math. Mech.* 100 (2020) e201900022, <https://doi.org/10.1002/zamm.201900022>.
- [34] C. van Erbruggen, C. Hirsch, M. Paiva, Anatomically based three-dimensional model of airways to simulate flow and particle transport using computational fluid dynamics, *J. Appl. Physiol.* 1985 (98) (2005) 970–980, <https://doi.org/10.1152/japplphysiol.00795.2004>.
- [35] B. Soni, A.K. Nayak, S. Wereley, A novel approach to quantify ventilation heterogeneity in occluded bronchial tree based on lung admittance, *Phys. Fluids* 34 (2022), <https://doi.org/10.1063/5.0085040>.
- [36] J. Alastruey, K.H. Parker, J. Peiró, S.J. Sherwin, Lumped parameter outflow models for 1-D blood flow simulations: effect on pulse waves and parameter estimation, *Commun. Comput. Phys.* 4 (2008) 317–336.
- [37] T.J. Pedley, R.C. Schroter, M.F. Sudlow, The prediction of pressure drop and variation of resistance within the human bronchial airways, *Respir. Physiol.* 9 (1970) 387–405, [https://doi.org/10.1016/0034-5687\(70\)90094-0](https://doi.org/10.1016/0034-5687(70)90094-0).
- [38] T. Mekonnen, X. Cai, C. Burchell, H. Gholizadeh, S. Cheng, A review of upper airway physiology relevant to the delivery and deposition of inhalation aerosols, *Adv. Drug Deliv. Rev.* 191 (2022) 114530, <https://doi.org/10.1016/j.addr.2022.114530>.
- [39] S. Ghosh, J.A. Ohar, M.B. Drummond, Peak inspiratory flow rate in chronic obstructive pulmonary disease: implications for dry powder inhalers, *J. Aerosol Med. Pulm. Drug Deliv.* 30 (2017) 381–387, <https://doi.org/10.1089/jamp.2017.1416>.
- [40] H. Jasak, A. Jemcov, Ž. Tuković, OpenFOAM: A C++ Library for Complex Physics Simulations, 2007, pp. 1–20.
- [41] Z. Zhang, C. Kleinstreuer, Laminar-to-turbulent fluid–nanoparticle dynamics simulations: model comparisons and nanoparticle-deposition applications, *Int. J. Numer. Methods. Biomed. Eng.* 27 (2011) 1930–1950, <https://doi.org/10.1002/cnm.1447>.
- [42] F.R. Menter, M. Kuntz, R. Langtry, Ten years of industrial experience with the SST turbulence model, *Turbul. Heat. Mass Tran.* 4 (2003) 625–632.
- [43] K. Ahookhosh, M. Saidi, H. Aminfar, M. Mohammadpourfard, H. Hamishehkar, S. Yaqoubi, Dry powder inhaler aerosol deposition in a model of tracheobronchial airways: validating CFD predictions with in vitro data, *Int. J. Pharm.* 587 (2020) 119599, <https://doi.org/10.1016/j.ijpharm.2020.119599>.
- [44] J. Zhao, Y. Feng, G. Tian, C. Taylor, N.S. Arden, Influences of puff protocols and upper airway anatomy on cannabis pharmacokinetics: a CFPD-PK study, *Comput. Biol. Med.* 132 (2021) 104333.
- [45] L. Chen, A. He, J. Zhao, Q. Kang, Z.-Y. Li, J. Carmeliet, N. Shikazono, W.-Q. Tao, Pore-scale modeling of complex transport phenomena in porous media, *Prog. Energy Combust. Sci.* 88 (2022) 100968, <https://doi.org/10.1016/j.pecc.2021.100968>.
- [46] K. Pradhan, A. Guha, Fluid dynamics of oscillatory flow in three-dimensional branching networks, *Phys. Fluids* 31 (2019).
- [47] P.W. Longest, J. Xi, Effectiveness of direct Lagrangian tracking models for simulating nanoparticle deposition in the upper airways, *Aerosol. Sci. Technol.* 41 (2007) 380–397, <https://doi.org/10.1080/02786820701203223>.
- [48] C. Kleinstreuer, Y. Feng, Computational analysis of non-spherical particle transport and deposition in shear flow with application to lung aerosol dynamics—a review, *J. Biomech. Eng.* 135 (2013) 21008, <https://doi.org/10.1115/1.4023236>, 021008.
- [49] A.A. Amsden, T.D. Butler, P.J. O'Rourke, The KIVA-II computer program for transient multidimensional chemically reactive flows with sprays, *SAE Trans.* (1987) 373–383.
- [50] A. Li, G. Ahmadi, Dispersion and deposition of spherical particles from point sources in a turbulent channel flow, *Aerosol. Sci. Technol.* 16 (1992) 209–226, <https://doi.org/10.1080/02786829208959550>.
- [51] A. Guha, Transport and deposition of particles in turbulent and laminar flow, *Annu. Rev. Fluid Mech.* 40 (2008) 311–341, <https://doi.org/10.1146/annurev.fluid.40.111406.102220>.
- [52] C.C. Miller, J. Walker, The Stokes-Einstein law for diffusion in solution, *Proc. R. Soc. Lond. - Ser. A Contain. Pap. a Math. Phys. Character* 106 (1997) 724–749, <https://doi.org/10.1098/rspa.1924.0100>.
- [53] J. Wang, R.C. Flagan, J.H. Seinfeld, Diffusional losses in particle sampling systems containing bends and elbows, *J. Aerosol Sci.* 33 (2002) 843–857, [https://doi.org/10.1016/S0021-8502\(02\)00042-3](https://doi.org/10.1016/S0021-8502(02)00042-3).
- [54] P. Cerretelli, R.S. Sikand, L.E. Farhi, Effect of increased airway resistance on ventilation and gas exchange during exercise, *J. Appl. Physiol.* 27 (1969) 597–600, <https://doi.org/10.1152/jappl.1969.27.5.597>.
- [55] R.E. Hyatt, R.E. Wilcon, The pressure-flow relationships of the intrathoracic airway in man, *J. Clin. Investig.* 42 (1963) 29–39, <https://doi.org/10.1172/JCI104693>.
- [56] N. Jahani, S. Choi, J. Choi, B. Haghighi, E.A. Hoffman, A.P. Comellas, J.N. Kline, C.-L. Lin, A four-dimensional computed tomography comparison of healthy and asthmatic human lungs, *J. Biomech.* 56 (2017) 102–110, <https://doi.org/10.1016/j.jbiomech.2017.03.012>.
- [57] D.J. Ross, P.F. Waters, A.D. Waxman, S.K. Koerner, Z. Mohsenifar, Regional distribution of lung perfusion and ventilation at rest and during steady-state exercise after unilateral lung transplantation, *Chest* 104 (1993) 130–135, <https://doi.org/10.1378/chest.104.1.130>.
- [58] N. Poord, A. Black, M. Walsh, Regional deposition of 2.5–7.5 μm diameter inhaled particles in healthy male non-smokers, *J. Aerosol Sci.* 9 (1978) 343–357, [https://doi.org/10.1016/0021-8502\(78\)90037-X](https://doi.org/10.1016/0021-8502(78)90037-X).
- [59] Y.-S. Cheng, Y. Zhou, B.T. Chen, Particle deposition in a cast of human oral airways, *Aerosol Sci. Technol.* 31 (1999) 286–300, <https://doi.org/10.1080/027868299304165>.
- [60] Y.-S. Cheng, Y. Yamada, H.-C. Yeh, D.L. Swift, Deposition of ultrafine aerosols in a human oral cast, *Aerosol. Sci. Technol.* 12 (1990) 1075–1081, <https://doi.org/10.1080/02786829008959417>.

Nomenclature

- Q : Volume flow rate
 P : Pressure
 D_t : Hydraulic diameter of throat
 D_{in} : Hydraulic diameter of inlet
 R : Flow resistance
 L : Length of throat
 d_p : Diameter of particle
 t : Time
CFPD: Computational fluid particle dynamics
EBN: Extended-Bronchial tree-Network
UP: Uniform pressure
 Stk : Stokes number
 Re : Reynolds number
 P_{EBN} : Pressure at the truncated branches with EBN boundary condition
 Q_{EBN} : Flow rate at the truncated branches with EBN boundary condition
 Q_b : Flow rate at the truncated branches using CFPD
 P_b : Pressure at the truncated branches using CFPD
TLB: Trachea to lobar bronchi
RUL: Right upper lobe
RML-RLL: Right middle lobe and right lower lobe
LUL: Left upper lobe
LLL: Left lower lobe
CFD: Computational fluid dynamics
PNM: Pore network model
 m_p : Mass of particle
 u : Velocity
 F_D^p : Drag force
 C_D : Drag coefficient
 ρ : Density
 C_C : Cunningham coefficient
 λ : Mean free path of molecule
 F_b^p : Buoyant force
 μ : Dynamic viscosity
 ν : Kinematic viscosity
RMS: Root mean square
 ν_t : Turbulence viscosity

k : Average kinetic energy
 F_i^{BM} : Brownian force
 T : Temperature of fluid
 G_i : Zero mean variant from a Gaussian probability density function
 S_m : Spectral intensity function
 D_m : Diffusion coefficient of particle
 DF : Deposition fraction
 DE : Deposition efficiency
 PF : Penetration fraction
 PF_{RD} : Relative disparity of PF using EBN method and UP method
 DF_{RD} : Relative disparity of DF using EBN method and UP method

N : Number of particles
 PF_{RD} : Relative disparity of PF using EBN method and UP method
 DF_{RD} : Relative disparity of DF using EBN method and UP method
 LPM : Liters per minute
 β : Momentum relaxation time of diffusion
 γ : Correlation coefficient of Poiseuille flow
 k_b : Boltzmann constant
 G_i : Zero mean variant from a Gaussian probability density function
 u_i' : Eddy velocity
 v_{rms} : Root mean square of the fluid isotropic fluctuating velocity
 MSD : Mean Squared Displacement